Journal of Water Process Engineering 78 (2025) 108642

Contents lists available at ScienceDirect

Journal of Water Process Engineering

journal homepage: www.elsevier.com/locate/jwpe

Enhanced flux of nanofiltration membranes for low molecular weight solutes using Zr-MOF@MoS_2 nanohybrids as both interlayer and filler materials

Javier Colás-Sebastián [a,b,1], José Miguel Luque-Alled [a,b,*,1], Carlos Téllez [a,b], Joaquín Coronas [a,b,*]

[a] Instituto de Nanociencia y Materiales de Aragón (INMA), CSIC-Universidad de Zaragoza, 50018 Zaragoza, Spain
[b] Departamento de Ingeniería Química y Tecnologías del Medio Ambiente, Universidad de Zaragoza, 50009 Zaragoza, Spain

ARTICLE INFO

Editor: Luca Fortunato

Keywords:
Thin film nanocomposite membrane
Polyamide
Zirconium metal-organic framework
MoS2
Water nanofiltration
Dye removal

ABSTRACT

This study investigates the fabrication and performance of polyamide (PA) thin film composite (TFC) membranes for nanofiltration applications, incorporating nanosized (~10 nm) zirconium-based metal-organic frameworks (MOFs) and MoS_2. Three different Zr-MOFs, namely UiO-66, UiO-66-NH_2 and MOF-808, were synthesized and anchored onto 2D MoS_2 nanosheets forming MOF@MoS_2 nanohybrids. These nanohybrids were integrated into PA TFC membranes using two distinct methods: (i) embedding them into the PA layer, resulting in thin film nanocomposite (TFN) membranes, and (ii) creating bilayered membranes with the nanohybrids beneath the PA layer. The membranes were evaluated for the removal of organic dyes, such as Rose Bengal (RB, 1017 Da), Sunset Yellow (SY, 452 Da) and Acridine Orange (AO, 265 Da), from water. The TFN membranes containing UiO-66@MoS_2 nanohybrids exhibited the highest performance, with a water permeance of 12 $L{\cdot}m^{-2}{\cdot}h^{-1}{\cdot}bar^{-1}$ for the SY dye solution, representing a 140 % increase relative to the control PA TFC membrane. All membranes exhibited high rejection values (> 98 %), with performance strongly influenced by the dye size and charge. The characterization revealed that the porosity and sorption capacities of the nanohybrids are crucial to obtain more permeable membranes, but other factors such as negative surface charge, roughness and hydrophilicity play an important role.

1. Introduction

Nanofiltration (NF) is a well-established membrane technology that effectively removes low molecular weight (MW) molecules and divalent salts from both water and organic solvents. Therefore, NF has been extensively investigated for various industrial processes requiring molecular separations from water, including the removal of organic and inorganic pollutants, as well as product isolation and processing in food technology and the pharmaceutical industry [1,2]. Most commercial NF membranes utilize a thin film composite (TFC) configuration, consisting of a 20–200 nm thick polyamide (PA) layer over a highly permeable, porous polymer support that provides a low transport resistance and a robust mechanical stability [2]. The ultrathin PA layer ensures high water flux, while its highly cross-linked structure delivers excellent rejection properties. However, the performance of NF membranes can be further enhanced by the addition of various nanomaterials [1]. PA TFCs exhibit high rejections of low MW organic molecules and divalent salts. Consequently, the research aimed at improving the performance of these membranes for NF applications mostly focuses on enhancing water flux. The incorporation of nanomaterials, such as metal-organic frameworks (MOFs) and 2D materials, has proven to be an effective strategy for achieving this goal. Nanomaterials can be incorporated in two distinct configurations: a thin film nanocomposite (TFN) configuration, where nanoparticles (NPs) are embedded within a polymer matrix, and a bilayer configuration, featuring two distinct layers of nanomaterial and polymer [3,4].

MOFs are particularly promising due to their high crystallinity and porosity, well-defined pore sizes, ease of synthesis and tunable functionalities [5]. Their high sorption capacities, coupled with the hydrophilicity in some cases, facilitate the interaction between the membrane and water molecules, thereby enhancing water permeation [2,6].

* Corresponding authors at: Instituto de Nanociencia y Materiales de Aragón (INMA), CSIC-Universidad de Zaragoza, 50018 Zaragoza, Spain.
E-mail addresses: jose.luque@unizar.es (J.M. Luque-Alled), coronas@unizar.es (J. Coronas).
[1] Both authors contributed equally to this work.

https://doi.org/10.1016/j.jwpe.2025.108642
Received 30 June 2025; Received in revised form 26 August 2025; Accepted 28 August 2025
Available online 5 September 2025

Abbreviations

AFM	atomic force microscopy
AO	Acridine Orange
BET	Brunauer–Emmett–Teller
DMSO	dimethyl sulfoxide
EDX	energy-dispersive X-ray spectroscopy
HDA	hexanediamine
HR-TEM	high-resolution transmission electron microscopy
IP	interfacial polymerization
IPA	isopropanol
MPD	phenylenediamine
MOF	metal-organic framework
MWCO	Molecular Weight Cut-Off
NF	nanofiltration
NPs	Nanoparticles
PA	polyamide
RA	Roughness average
RB	Rose Bengal
RMS	Root mean square
SEM	scanning electron microscopy
SSA	Specific Surface Area
STEM-HAADF	scanning transmission electron microscopy-high-angle annular dark-field
SY	Sunset Yellow
TFC	thin film composite
TFN	thin film nanocomposite
TGA	thermogravimetric analysis
TMC	trimesoyl chloride
UV–Vis	ultraviolet-visible spectroscopy
WCA	water contact angle
XPS	X-ray photoelectron spectroscopy
XRD	X-ray diffraction

Furthermore, their open and porous structure provides new and faster transport routes for water molecules, thus enhancing the overall water diffusivity through the membrane [3,7]. Nevertheless, integrating MOFs into the organic polymer matrix presents a significant challenge due to the deficient compatibility between the rigid, discrete particles and the flexible organic polymer chains with distinct chemistries [8]. This frequently results in the uncontrolled formation of voids at the polymer/MOF interface. The presence of these additional voids can facilitate permeation by creating pathway shortcuts through the polymer/MOF interface. However, if these voids become too large, which is likely given their uncontrolled nature, they can allow the transport of undesired molecules, thereby reducing rejection efficiency. To mitigate this disadvantage, MOFs are often chemically modified to enhance their compatibility with the polymer [8,9], frequently altering their original porosity properties. Among the existing MOFs, those containing zirconium (Zr) as the metallic center and carboxylate-based linkers have garnered significant attention for water-related applications. UiO-66 (University of Oslo), synthesized using Zr(IV) and 1,4-benzenedicarboxylate ligand, is the most renowned of its kind. It features a pore volume of 0.77 $cm^3 \cdot g^{-1}$, a pore aperture of 0.6 nm, a specific surface area (SSA) of 1160 $m^2 \cdot g^{-1}$ and it shows a hydrophilic behavior due to the presence of carbonyl groups and unsaturated Zr(IV) sites [10]. For instance, Ma et al. showed that the incorporation of UiO-66 nanoparticles into PA TFCs increased water permeability by 52 % and maintained salt rejection at 95 % [11]. A derivative known as UiO-66-NH_2 exhibits an enhanced hydrophilicity, resulting from the incorporation of an amine group into the benzene ring [6]. In fact, several authors have investigated the use of this MOF for water NF applications [6,12]. Another alternative is MOF-808, which also contains a Zr(IV) metal center, but uses a benzene ring with three carboxyl groups (trimesate ligand) as a ligand resulting in 8-connected Zr_6 nodes, compared to the two carboxyl groups in UiO-66 (12-connected Zr_6 nodes). This difference leads to distinct crystal packing, resulting in different porosity and surface area; MOF-808 having a pore volume of 0.76 $cm^3 \cdot g^{-1}$, pore apertures of 0.48 and 1.8 nm and a SSA value of ~1200 $m^2 \cdot g^{-1}$ [13,14].

Particularly interesting is the synthesis of nanosized MOFs [18]. In spherical particles, the ratio of external surface area to volume increases as the particle size decreases. Consequently, these nanosized or ultrasmall particles exhibit a greater number of attractive interactions compared to their larger counterparts, thereby increasing membrane permeation. Recently, ultrasmall particles have been synthesized using an oxocluster as a precursor [19–22], although their potential for use in water NF applications has barely been investigated. Ultrasmall UiO-66-NH_2 NPs were embedded in a thin PA layer on a polydopamine-coated carbon nanotube film to form a TFN membrane [23]. This membrane achieved a water permeance of 46 $L \cdot m^{-2} \cdot h^{-1} \cdot bar^{-1}$ and Na_2SO_4 rejection of 97.1 %; i.e. a 53 % increase in permeance compared to the TFC membrane. Therefore, the investigation of ultrasmall nanoparticles (NPs) for water-related applications remains limited. To enable a high loading of these NPs, their immobilization onto 2D nanosheets presents a promising strategy, offering a more robust method for incorporating ultrasmall NPs into PA layers. 2D materials have garnered considerable interest over recent decades. Their distinctive structure allows for a very high aspect ratio, imparting substantial surface properties [24]. Particularly 2D MoS_2 nanolaminates have been used to obtain improved NF TFN membranes but it has been necessary to treat, modify or functionalize them with other compounds such as polydopamine [25], 1,3-propane sulfone [26], tannic acid [27] or acyl chloride [28]. 2D materials serve as excellent platforms for the deposition of various materials, including MOFs [29–32]. This represents an effective approach to preventing MOF aggregation and ensuring a significant surface area of the MOF is available for interaction with water molecules [33].

Here, we report the synthesis of ultrasmall MOFs on the basal plane of 2D MoS_2 nanosheets and their role as nanofillers in PA NF membranes. These three Zr-based MOFs (see Table 1) are among the most relevant in the field. UiO-66 is the most studied and is considered the archetypal Zr-MOF. UiO-66-NH_2 is structurally similar to UiO-66 but exhibits enhanced hydrophilicity due to the presence of amino groups in the MOF linker. MOF-808 was selected because, although it shares similar chemistry to UiO-66, it differs in connectivity (8-connected vs. 12-connected), which significantly alters its overall structure and porosity. MoS_2 nanosheets enable attractive interactions with metal cations, facilitating the fabrication of these MOFs on the 2D material. The MOF@MoS_2 nanohybrid was utilized to prepare both TFN and

Table 1
Comparison of porosity and surface area of the Zr-MOFs used in this work: UiO-66 [10], UiO-66-NH_2 [15–17], and MOF-808 [13,14]. As the surface area and pore volume are highly dependent on the synthetic conditions, the values shown are representative examples and may vary with different synthesis procedures. Fig. S1 shows organic linkers used to prepare UiO-66, UiO-66-NH_2, and MOF-808.

MOF	Connected Zr_6 nodes	BET specific surface area ($m^2 \cdot g^{-1}$)	Pore aperture (nm)	Pore volume ($cm^3 \cdot g^{-1}$)
UiO-66	12	~1160	0.6	~0.77
UiO-66-NH_2	12	~900	0.6	~0.38–0.5
MOF-808	8	~1200	0.48 and 1.8	~0.5–0.76

bilayered membranes. P84® (polyimide) supports were employed due to their strong chemical resistance, commercial availability, and their ability to withstand dimethyl sulfoxide (DMSO) treatment, which plays a key role in opening the pores of the PA layer and thus enhancing membrane permeation. In contrast, other commercially available supports such as Polysulfone (PSF) and polyethersulfone (PES) are not suitable due to their instability in DMSO. All membranes were characterized using scanning electron microscopy (SEM), atomic force microscopy (AFM), water contact angle (WCA), X-ray photoelectron spectroscopy (XPS), transmission electron microscopy (TEM), molecular weight cut-off (MWCO) and zeta potential measurements. All membranes were evaluated for the removal of low MW organic dye molecules such as Rose Bengal (RB, 1017 Da), Sunset Yellow (SY, 452 Da) and Acridine Orange (AO, 265 Da). To the best of our knowledge, the closest precedent using analogous materials focused on the application of UiO-66-NH_2@MoS_2 as an interlayer to adjust the properties of the substrate for forward osmosis applications [33], that is neither addressing the NF application nor comparing different Zr-MOF ultrasmall NPs and membrane configurations.

2. Material and methods

2.1. Materials

The following chemicals were employed for the synthesis of MOF@MoS_2 nanohybrids: zirconium (IV) chloride ($ZrCl_4$, 99.9 %), glacial acetic acid (HA, >99 %), MoS_2 powder, 1,4-dicarboxylic acid (synthesis grade), 2-aminobenzene-1,4-dicarboxylic acid (99 %) and benzene-1,3,5-tricarboxylic acid (98 %) (see Fig. S1) and n-hexane were obtained from Merck. Methanol (HPLC grade) and isopropanol (IPA, 99.9 %) was purchased from Análisis Vínicos (Spain). All materials were used as received.

The fabrication of the P84® (polyimide) supports and the synthesis of polyamide (PA) layers were carried out using the following reagents and solvents: polypropylene nonwoven backing material from Freudenberg Performance Materials, P84® powder (200 mesh) from HP Polymer GmbH and dimethyl sulfoxide (DMSO, 99.8 %) from Carlo Erba Reagents. Hexanediamine (HDA, 98 %), phenylenediamine (MPD, 99 %), and trimesoyl chloride (TMC,98 %) were obtained from Merck. Polyethylene glycol (PEG, synthesis grade) was acquired from Scharlau and absolute ethanol (EtOH) was procured from Gilca. For the NF experiments, the following chemicals were used: RB, (95 %, 1017 Da), SY, (90 %, 452 Da) and AO, (55 %, 265 Da) were all purchased from Merck. Deionized (DI) water with a conductivity of 1.35 $\mu S \cdot m^{-1}$ was used.

2.2. Synthesis of ultrasmall nanoparticles over MoS_2 nanosheets

Three types of MOFs were synthesized on the basal plane of MoS_2 nanosheets for comparison of their respective properties: (1) UiO-66, (2) UiO-66-NH_2 and (3) MOF-808. The initial step in this study involved the synthesis of the precursor for the MOFs, specifically Zr(IV) oxoclusters (see Section 2.2.1). The formation of these oxoclusters allows for precise control over the particle size of the MOFs, resulting in particularly small particles. Concomitant with this, nanosheets were exfoliated from a MoS_2 powder as the source material (see Section 2.2.2).

2.2.1. Synthesis of Zr(IV) oxoclusters

The synthesis is conducted in accordance with the procedure described by Martinez-Izquierdo et al. [34] A solution was prepared by mixing 5 mL of IPA with 3 mL of AcH, to which 2 g of $ZrCl_4$ were added. The mixture was stirred magnetically until the $ZrCl_4$ was completely dissolved. The reaction was carried out in an autoclave at 120 °C for 1 h. The resulting white solid was then washed to remove any unreacted compounds by centrifugation (10,000 rpm for 20 min each) using acetone (three washes in overall). After washing, the solid product was dried at room temperature (RT) for 24 h.

2.2.2. Exfoliation of MoS_2 nanosheets

A suspension of exfoliated MoS_2 was prepared by dispersing 1.8 g of MoS_2 powder in 180 mL of ethanol. The dispersion was sonicated for 24 h at RT using an ultrasonic bath. Subsequently, the resulting suspension was subjected to centrifugation at 10,000 rpm for 40 min, with the goal of separating the larger aggregates. The supernatant was carefully decanted, yielding a blueish suspension comprising the MoS_2 nanosheets dispersed in ethanol. The aforementioned suspension was employed as the substrate for the subsequent synthesis of ultrasmall MOFs on the basal plane of MoS_2 nanosheets.

2.2.3. UiO-66@MoS_2 nanohybrids (UiO-66@MoS_2)

0.3 g of Zr(IV) oxocluster were dispersed in 2 mL of acetic acid through magnetic stirring. Subsequently, 5 mL of distilled water was added and the obtained mixture was stirred until it becomes colorless. This solution was then mixed with the MoS_2 nanosheets and stirred for 30 min. Subsequently, 200 mg (1.2 mmol) of 1,4-dicarboxylic acid was added and the mixture was stirred for 2 h at RT. This resulted in the metal-coordinated acetate molecules in the oxocluster being replaced by the ligand, thereby forming the MOF while essentially maintaining the size of the Zr(IV) oxocluster. Upon completion of the reaction, the solid was recovered by centrifugation at 10,000 rpm for 45 min and washed three times with ethanol by centrifugation (10,000 rpm, 45 min). Finally, the solid was dried in an oven at 40 °C overnight.

2.2.4. UiO-66-NH_2@MoS_2 nanohybrids (UiO-66-NH_2@MoS_2)

The synthesis of UiO-66-NH_2@MoS_2 nanohybrids followed the same procedure as that of UiO-66@MoS_2, but 1,4-dicarboxylic acid was replaced with 2-aminobenzene-1,4-dicarboxylic acid (220 mg, 1.2 mmol).

2.2.5. MOF-808@MoS_2 nanohybrids (MOF-808@MoS_2)

The procedure was identical to that described for UiO-66@MoS_2, with the exception that benzene-1,3,5-tricarboxylic acid (253 mg, 1.2 mmol) was employed as a ligand.

2.3. Membrane fabrication

All membranes were utilized within a period of no more than 5 d from the time of preparation. The fabricated membranes and manufacturing details of all membranes can be found in Fig. 1 and Table 2.

2.3.1. Thin film composite membranes (TFCs)

PA layers were synthesized over cross-linked P84® supports using the conventional interfacial polymerization (IP) technique. The fabrication of P84® supports is described in our previous publication [3], but 22 wt% loading of P84® in the dope solution was employed. The IP was conducted as follows: first, the P84® support was impregnated with an aqueous solution of 2 % ($w \cdot v^{-1}$) MPD (10 mL) for a period of 2 min. Then, the surplus solution was eliminated through the utilization of a rubber brayer roller and a spraying process with compressed air for a period of 10 s. Then, a solution of 10 mL of 0.1 % ($w \cdot v^{-1}$) TMC in n-hexane was applied to the impregnated P84® support for 2 min to allow IP and the formation of the PA TFC. The resulting membrane was washed with n-hexane (10 mL, twice) and water (10 mL, once) to remove any excess TMC. They were then stored in a Petri dish with DI water at 4 °C until required.

2.3.2. Thin film nanocomposite membranes

TFN membranes were prepared by adding 0.01 % ($w \cdot v^{-1}$) of MOF@MoS_2 nanohybrids to the MPD (2 % $w \cdot v^{-1}$) aqueous solution. Thus, the MOF@MoS_2 nanohybrids were incorporated to the P84® supports and the IP occurred between MPD and TMC molecules wrapping the 2D MOF@MoS_2 nanosheets (Fig. 1).

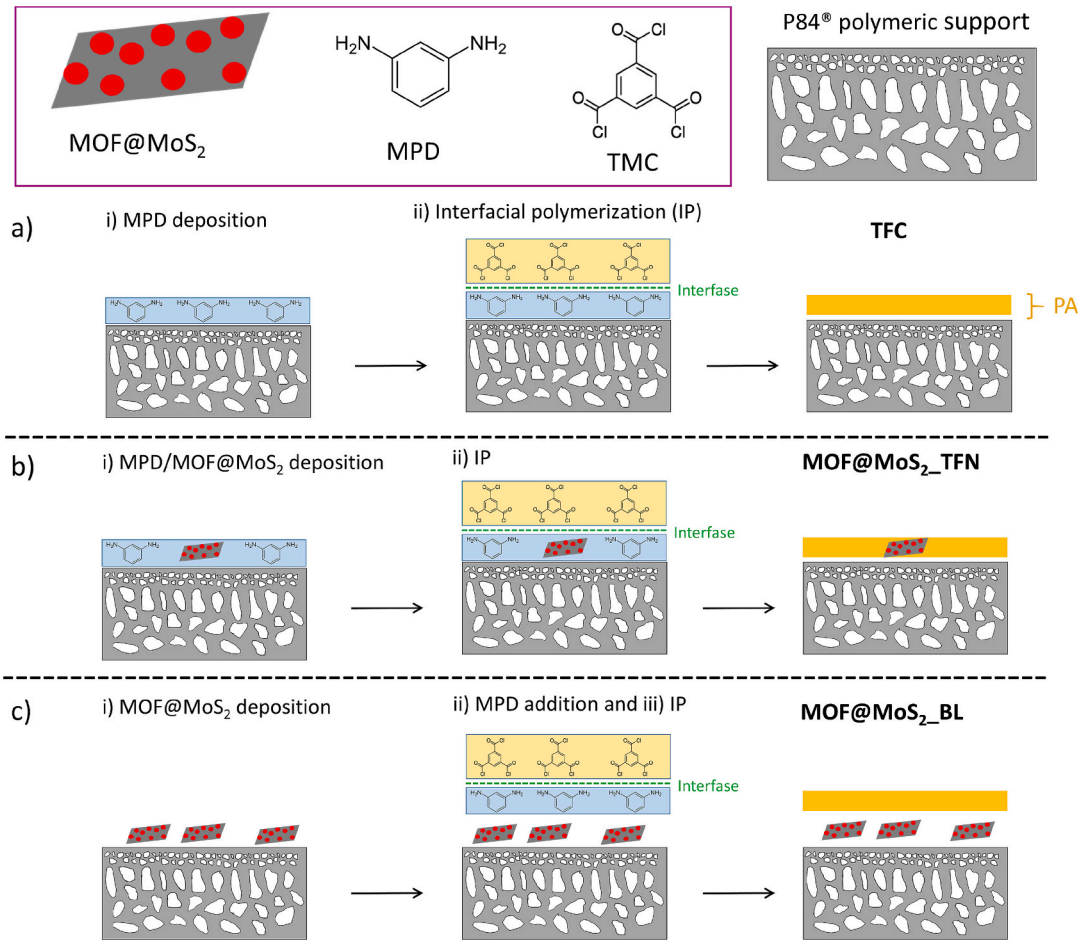

Fig. 1. Fabrication of TFCs (a), MOF@MoS_2_TFN (b) and MOF@MoS_2_BL membranes (c).

Table 2
Fabrication details of all prepared membranes encompassing membrane code, MOF@MoS_2 nanohybrid and membrane configuration.

Membrane code	Membrane configuration	MOF@MoS_2 nanohybrid	Nanohybrid concentration[a]
PA_TFC	TFC	–	–
U66@MoS_2_TFN	TFN	UiO-66@MoS_2	0.1 mg·mL^{-1}
U66-NH_2@MoS_2_TFN	TFN	UiO-66-NH_2@MoS_2	0.1 mg·mL^{-1}
M808@MoS_2_TFN	TFN	MOF-808@MoS_2	0.1 mg·mL^{-1}
U66@M_BL (Evap_1)	Bilayer (evaporation)	UiO-66@MoS_2	1 mg·mL^{-1}
U66@M_BL (Evap_0.1)	Bilayer (evaporation)	UiO-66@MoS_2	0.1 mg·mL^{-1}
U66@M_BL (SC_0.1)	Bilayer (spin coating)	UiO-66@MoS_2	0.1 mg·mL^{-1}

[a] In TFNs this concentration corresponds to the aqueous solution containing MPD; in bilayered membranes, this corresponds to the solution used to prepare the nanohybrid layer prior to IP.

2.3.3. Bilayered membranes (BL)

TFN membranes named as bilayered membranes (BL) were prepared by first depositing MOF@MoS_2 nanosheets on the P84® support, followed by the synthesis of a PA layer on top (MOF@MoS_2_BL in Fig. 1). MOF@MoS_2 nanosheets were deposited using two different methods: evaporation and spin-coating.

In the evaporation method, a MOF@MoS_2 suspension (1 or 0.1 mg·mL^{-1} in IPA) was prepared and 1 mL of this suspension was added to the pre-heated (80 °C) surface of the P84® support. The membrane was then subjected to heating at 80 °C for 5 min until the IPA evaporated, thereby leaving MOF@MoS_2 nanosheets on top of the support. In the case of the spin-coating method, 1 mL of a MOF@MoS_2 suspension (0.1 mg·mL^{-1}) in IPA was spin coated on top of the P84® support.

2.4. Characterization

MOF@MoS_2 nanohybrids were characterized using the following techniques. Thermogravimetric analysis (TGA) was performed using a Mettler Toledo TGA/STDA 851e instrument. Approximately 3 mg of the nanohybrid sample powder was placed in an alumina pan (70 μL) and heated under an airflow of 40 $cm^3 \cdot min^{-1}$ (STP) from 35 to 700 °C at a heating rate of 10 °C·min^{-1}. X-ray diffraction (XRD) measurements were conducted using a PANalytical Empyrean-Multipurpose device (Malvern Panalytical Ltd) equipped with a Cu Kα rotating anode (λ = 1.1542 Å), operating at 40 kV and 80 mA. A reflection-transmission spinner stage with a zero-background sample holder was employed for XRD analysis. High resolution-transmission electron microscopy (HR-TEM) images were captured using a Thermo Fisher Scientific Titan Analytical at an accelerating voltage of 300 kV equipped with an energy-dispersive X-ray (EDX) detector, employing holey carbon support films on a copper 300 square mesh (Aname). Nitrogen adsorption-desorption isotherms were recorded using a Micromeritics Tristar 3000 working at −195.8 °C, the Brunauer-Emmett-Teller (BET) specific surface area (SSA) being calculated with the Micromeritics software. Prior to analysis, samples were degassed under vacuum at 200 °C for 8 h with a heating rate of 10 °C·min^{-1}. Selected membranes were characterized using a range of techniques. SEM images were taken with a FEI-Inspect F20 microscope operating at 30 kV and elemental analysis was obtained using an EDX

detector. WCA measurements were conducted using a Krüss Drop Shape Analyzer 10 MK2 at 25 °C. An average of three measurements per membrane code was reported along with its standard deviation. AFM analysis was performed at ambient pressure using a Bruker MultiMode 5 scanning probe microscope in tapping mode, with a scan rate of 1 Hz and an amplitude of approximately 250 mV. Analysis of roughness parameters was performed using the free user software Gwyddion. XPS measurements were obtained with a Kratos Axis Ultra spectrometer, utilizing a monochromatic Al Kα (1486.6 eV) X-ray source operating at 10 mA, 15 kV and 150 W. High resolution spectra (C1s, O1s, Zr3d, S2p and Mo3d) were analyzed with CASA XPS software. The zeta potential measurements were conducted using a SurPASS 3 Eco analyzer from Anton Paar. Membrane samples were prepared by cutting them into uniform rectangular sections and thoroughly rinsing them with deionized water before mounting into the testing cell. During the measurement, a 0.1 M KCl electrolyte solution, adjusted to a neutral pH of 7.0, was flowed through the membrane sample assembly. All measurements were performed three times to ensure accuracy and reproducibility. Molecular weight cut-off (MWCO) experiments were performed using aqueous PEG solutions (concentration of 5 $g{\cdot}L^{-1}$) of varying molecular weights: 200, 400, 600 and 1500 Da. The concentration of PEG in the retentate and permeate solutions were quantified using a Shimadzu TOC-L Series total organic carbon (TOC) analyzer. Ultrathin specimens of 70 nm of U66@MoS_2_TFN membranes were obtained by ultramicrotomy and imaged using a T20 Tecnai transmission electron microscope operating at 30 kV and equipped with an energy-dispersive X-ray detector, as described elsewhere [3].

2.5. Water nanofiltration experiments

NF experiments were conducted utilizing a Sterlitech HP4750 dead-end membrane module with aqueous dye solutions. Independent dye solutions of RB (MW = 1017 Da), SY (MW = 452 Da) and AO (MW = 265 Da) at a concentration of 20 $mg{\cdot}L^{-1}$ each were employed. The experiments were carried out under a feed pressure of 20 bar and maintained at 20 °C. A membrane with an effective area of 4.9 cm^2 was used, along with a feed volume of 250 mL. Prior to filtration of the dye solution, the membrane was washed with DMSO for 1 h at 20 bar. This process was employed to remove any residual monomers and facilitate the swelling of the polymer chains. Afterwards, the membrane surface was rinsed with abundant DI water. Filtration with dye solutions was conducted for a period of 1–2 h until a stable flux was achieved, in order to facilitate membrane compaction. The permeance ($L{\cdot}m^{-2}{\cdot}h^{-1}{\cdot}bar^{-1}$) and rejection (%) used to evaluate membrane performance were calculated using the following equations [35]:

$$Permeance = \frac{V}{t{\cdot}A{\cdot}\Delta P} \tag{1}$$

$$Rejection\ (\%) = \left(1 - \frac{C_{permeate}}{C_{retentate}}\right){\cdot}100 \tag{2}$$

where V represents the permeate volume (L), A is the membrane area (m^2), t is the permeation time (h) and ΔP is the transmembrane pressure (bar). $C_{permeate}$ and $C_{retentate}$ account for the concentrations of dyes in the permeate and retentate side, respectively. The reported permeance and rejection values are mean values with their corresponding standard deviations of at least three different membranes tested. These concentrations were related to dye absorbance values, which were obtained by means of a UV–Vis Jasco V-670 spectrophotometer using quartz cuvettes and water as a solvent. Among the techniques employed, UV–Vis spectroscopy is a well-established method for the detection and quantification of organic pollutants [3,15]. Flux improvement was calculated as follows:

$$Permeance\ improvement\ (\%) = \left(\frac{Membrane\ permeance - TFC\ permeance}{TFC\ permeance}\right){\cdot}100 \tag{3}$$

3. Results

3.1. Characterization of UiO-66@MoS_2, UiO-66-NH_2@MoS_2 and MOF-808@MoS_2

The crystalline structure of all nanohybrids was analyzed through XRD. Fig. 2a provide comparative analyses of the nanohybrids against those of the individual MOFs and MoS_2 nanosheets and the corresponding simulations of each MOF. The XRD patterns for all samples show a significantly intense main peak of considerable width. This peak broadening is attributed to the small size of the nanoparticles (NPs) as a result of a limited number of atomic planes available to produce constructive interferences [19]. Additionally, ultrasmall NPs synthesized via the Zr oxocluster method are prone to minor structural defects, which may further contribute to the peak broadening [20]. Furthermore, the characterizations presented below, such as the BET specific surface area, XPS, TGA and TEM, support the formation of the MOF. All synthesized ultrasmall MOF NPs show a similar characteristic pattern with only one broad main intensity peak and the absence of other peaks, which is consistent with that reported in the literature for ultrasmall nanoparticles [19,20,36]. The main peak in the bulk MoS_2, which is attributed to stacked 2D laminates, is no longer discernible in the spectra of the nanohybrids. This evidence is consistent with a high efficacy of the exfoliation process [37].

The BET specific surface area (SSA) was employed to investigate the porosity of the synthesized nanohybrids (Fig. S2). The existence of micropores was observed in all samples, which is attributed to the presence of MOFs [19,38]. Additionally, some mesoporosity was observed, which is indicative of voids between NPs. The BET SSA values of the nanohybrids, 710 $m^2{\cdot}g^{-1}$ for UiO-66@MoS_2, 428 $m^2{\cdot}g^{-1}$ for UiO-66-NH_2@MoS_2 and 410 $m^2{\cdot}g^{-1}$ for MOF-808@MoS_2, are significantly reduced as compared to those of the bare MOFs (>1000 $m^2{\cdot}g^{-1}$ [10,13,14]) but still high in aggrement with the claimed micropores above. This finding aligns with the presence of laminar MoS_2, which has been observed to exhibit a markedly low N_2 sorption capability with BET SSA of 3.1 $m^2{\cdot}g^{-1}$ [31].

Fig. 2b illustrates the TGA curves of all nanohybrids, along with those of the MOF and MoS_2 samples. The curves of weight loss of all nanohybrids fall between those of MOFs and MoS_2, in agreement with the fact that they are composed of both. The final weight percentages of the nanohybrids at 700 °C were employed to calculate the MOF loadings. The values of MOF loading were as follows: 75 wt% for UiO-66@MoS_2, 85 wt% for UiO-66-NH_2@MoS_2 and 94 % for MOF-808@MoS_2.

XPS was employed to analyze the formation of UiO-66@MoS_2 by comparison with that of Zr(IV) oxocluster and UiO-66. The Zr(IV) oxocluster is mainly formed by acetate species and metal atoms. The formation of both UiO-66 and UiO-66@MoS_2 occurs through the replacement of the acetate specie by the 1,4-benzenedicarboxylate ligand. This chemical exchange is identified through the examination of the corresponding C 1 s high resolution spectra. The C-C/C-O ratio of both UiO-66@MoS_2 and UiO-66 is higher (4.7 and 4.8, respectively) than that of the Zr(IV) oxocluster (3.3), which can be attributed to the incorporation of the dicarboxylate ligand (Fig. S3). Moreover, the high resolution spectra of Mo 3d and S 2p for UiO-66@MoS_2 nanohybrids exhibit the characteristics of MoS_2 [39], indicating that the deposition of UiO-66 nanoparticles does not alter the chemical composition of the 2D material (Fig. S3).

Fig. 3a–d show the TEM images corresponding to the MOF@MoS_2 nanohybrids. These images reveal a granular structure that can be attributed to the presence of MOF NPs. Elemental mapping through EDX

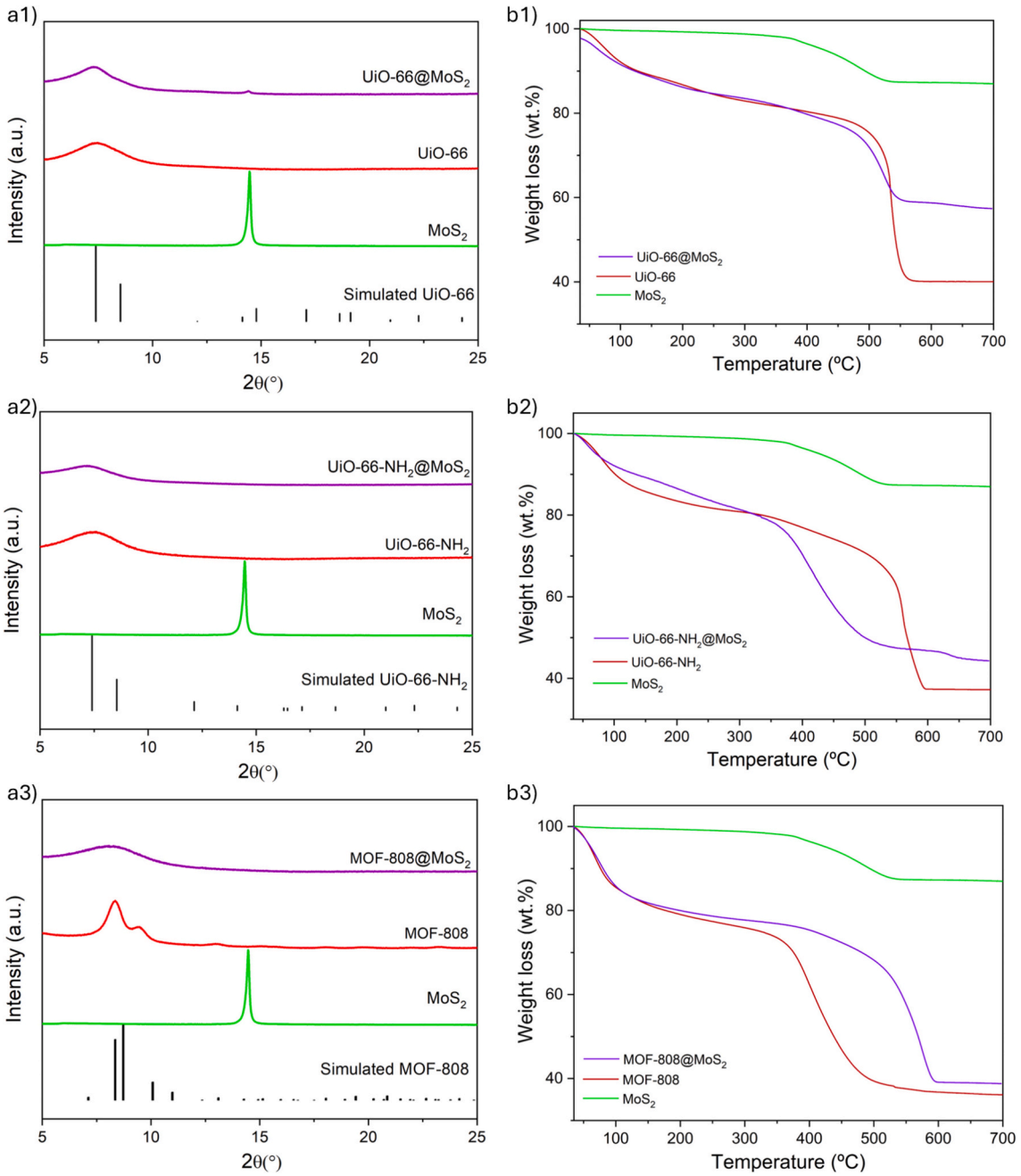

Fig. 2. XRD patterns (a) and TGA curves (b) of: MoS_2, UiO-66@MoS_2 (a1 and b1), UiO-66-NH_2@MoS_2 (a2 and b2) and MOF-808@MoS_2 (a3 and b3) nanohybrids and their corresponding MOF counterparts.

(Fig. 3e) provided further insights into the distribution of various elements within the sample and confirmed that the granular patterns correspond to ultrasmall UiO-66@MoS_2 particles. The analysis of oxygen, zirconium and carbon demonstrated the existence of nanoparticle clusters localized in specific regions. Conversely, the distributions of molybdenum and sulphur atoms appeared more homogeneous across the sample due to the presence of a 2D MoS_2 nanosheet. Fig. 3b demonstrates the successful exfoliation of MoS_2, as the resulting nanohybrids are composed of monolayer or few-layer MoS_2 nanosheets. Additional STEM-HAADF images and EDX analysis can be found in the supporting information. Fig. S4 shows that the edge of the 2D material, where few-layer laminates are observed, exhibits markedly higher intensities for molybdenum and sulphur atoms. Figs. S5 and S6 correspond to UiO-66-NH_2@MoS_2 and MOF-808@MoS_2 nanohybrids, respectively, the distribution of MOF nanoparticles being similar to that of UiO-66. In brief, in any of the MOF@MoS_2 nanohybrids, NPs with sizes around 10 nm are identified, which implies the preservation of the laminar character of MoS_2 and its surface modification with a porous material with a different chemistry.

3.2. *Membrane characterization*

Top-view SEM images were employed to investigate the morphology of the membrane surface. As shown in Fig. 4, all membranes exhibit the distinctive ridge-and-valley morphology of PA TFCs [40,41]. The SEM image of the TFC membrane shows the presence of the characteristic ear-shaped features that are indicative of a fast IP reaction [3]. These features are less noticeable for the membranes incorporating the nanohybrids (Fig. 4b, c and d), concomitant with a reduction in surface roughness. This is primarily attributed to the influence of the 2D

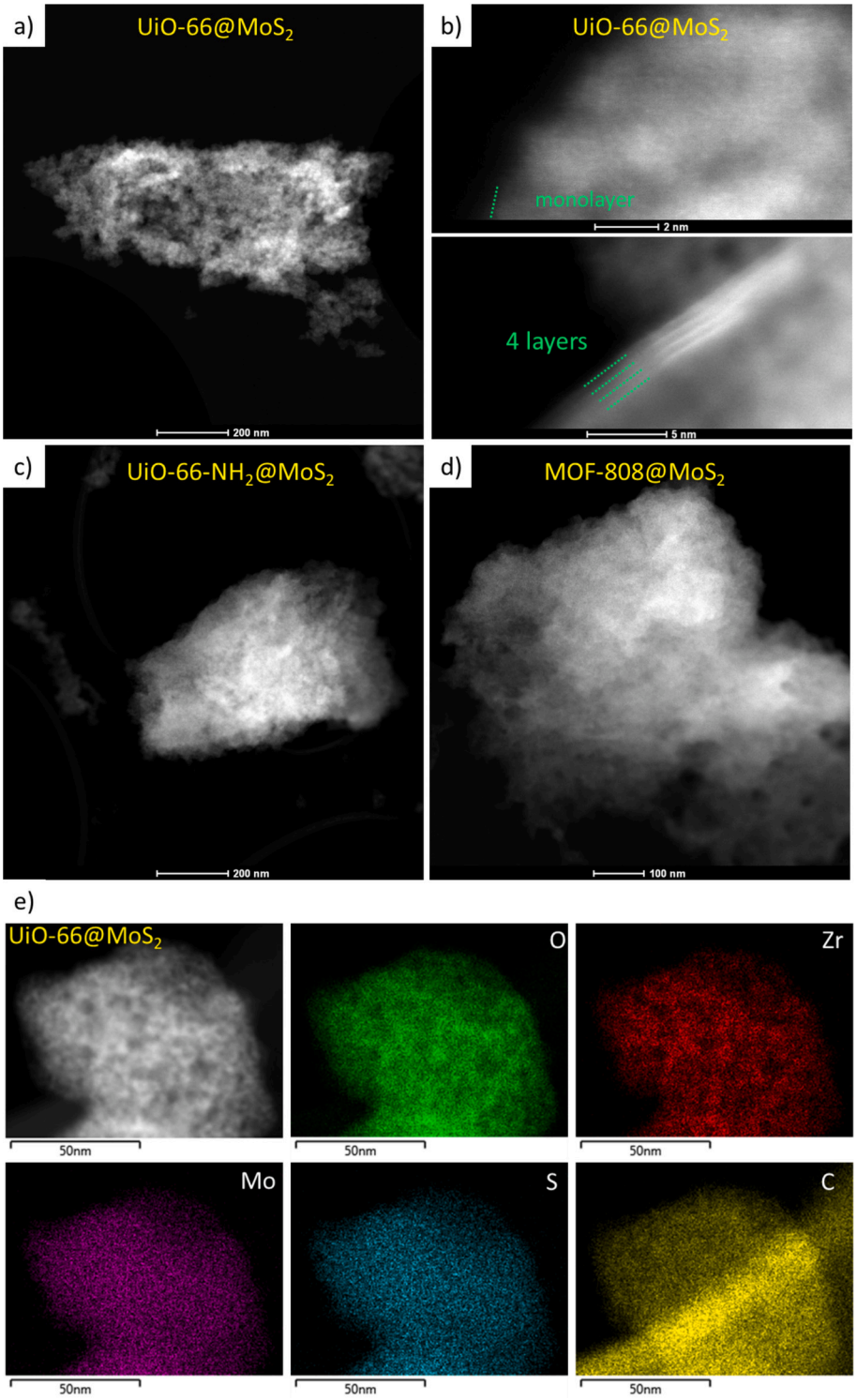

Fig. 3. STEM-HAADF images of UiO-66@MoS_2 (a and b), UiO-66-NH_2@MoS_2 (c), MOF-808@MoS_2 (d) and EDX analysis for UiO-66@MoS_2 (e).

nanosheets, thereby forming flatter surfaces and reducing surface irregularities. Besides, MOFs on the surface of the nanohybrids may interact with the monomers during the IP process. In fact, MPD may react with free carboxylic groups in the MOF, while TMC may bind to uncoordinated Zr^{4+} at defective sites (illustrated in Fig. 5). Moreover, ultrasmall nanoparticles synthesized via oxocluster formation exhibit a particularly high number of defect sites [21] and furthermore the porosity of the MOF can act as reservoirs of the monomers that slowly dose them. As a consequence of this, the IP reaction is slowed down, resulting in a reduction in the number of protrusions and lower surface roughness. The SEM image of the bilayered membrane (Fig. 4e) shows as well a markedly reduced surface roughness in comparison with PA_TFC, which can be primarily explained by the 2D nature of the nanohybrids and their position, more submerged in the polyamide (PA) layer, near the support surface, than in the TFN membrane.

AFM analysis was conducted to provide a comprehensive evaluation of the membrane surface roughness (Fig. S7). Quantitative evaluation of the mean roughness (Ra) and root mean square (RMS) values indicates

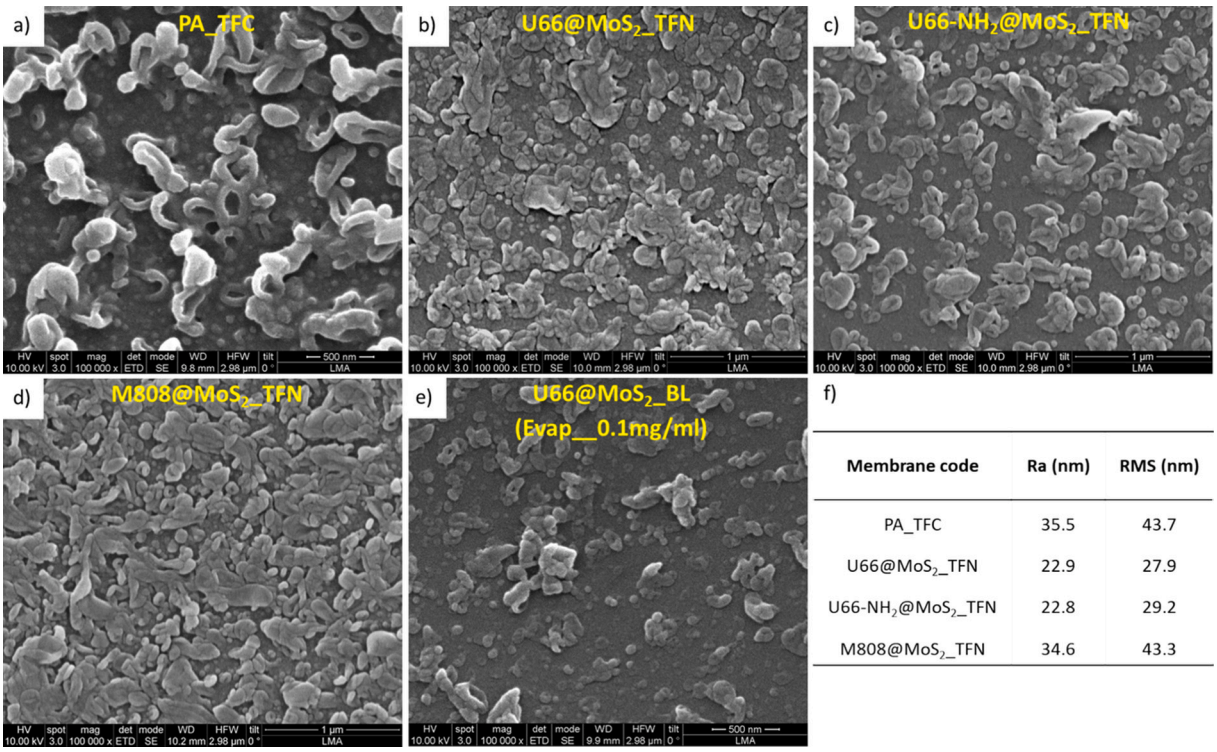

Membrane code	Ra (nm)	RMS (nm)
PA_TFC	35.5	43.7
U66@MoS_2_TFN	22.9	27.9
U66-NH_2@MoS_2_TFN	22.8	29.2
M808@MoS_2_TFN	34.6	43.3

Fig. 4. SEM images of PA_TFC (a), U66@MoS_2_TFN (b), U66-NH_2@MoS_2_TFN (c), M808@MoS_2_TFN (d), U66@MoS_2_BL (Evap_0.1) (e) and Ra and RMS parameters estimated from AFM (f).

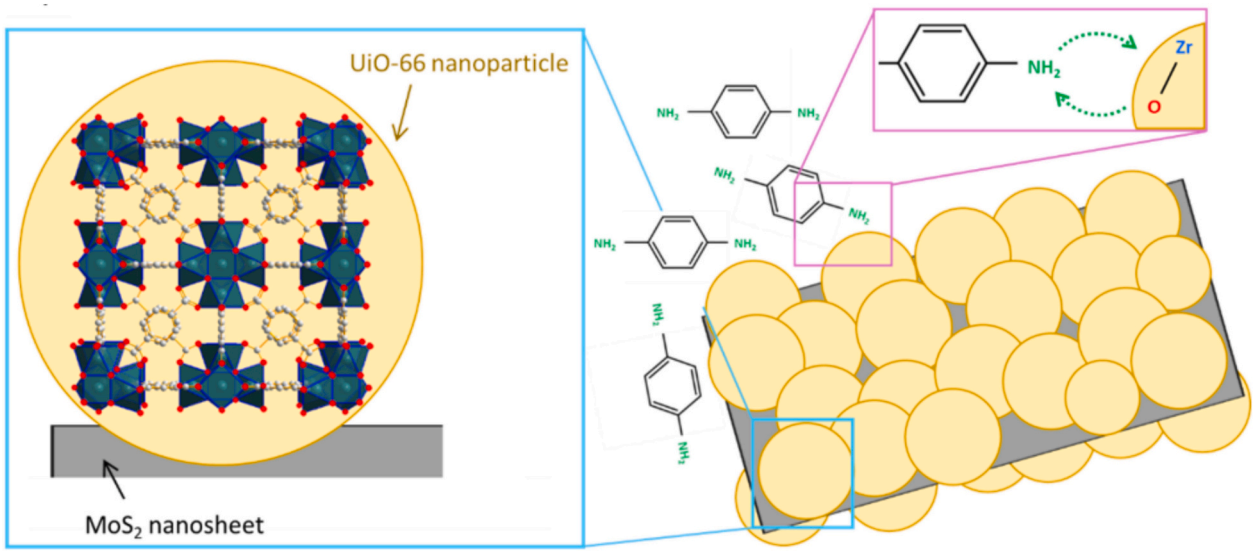

Fig. 5. Organic linkers used to prepare UiO-66, UiO-66-NH_2, and MOF-808 (a) and illustration of MOF-MPD interactions using UiO-66 as an example (b).

that higher values of these parameters correspond to more pronounced roughness (Fig. 4f). The highest values were obtained for PA_TFCs (Ra of 35.5 nm and RMS of 43.7), attributed to the large ear-shaped protuberances observed in the SEM images and mentioned above (e.g., ridge-and-valley morphologies). The incorporation of the nanohybrids into the membranes was found to result in a reduction in surface roughness, particularly for U66@MoS_2_TFN (Ra of 22.9 nm and RMS of 27.9) and U66-NH_2@MoS_2_TFN (Ra of 22.8 nm and RMS of 29.2). The exception is M808@MoS_2_TFN (34.6 nm for Ra and 43.4 nm for RMS), which has very similar values to those of the TFC. SEM images of this particular TFN (Fig. 4d) reveal a significantly higher density of protuberances compared to other TFNs, which accounts for its increased roughness. This phenomenon may be attributed to the larger pore aperture and pore volume of MOF-808 (1.8 nm) compared to MOFs UiO-66 and UiO-66-NH_2 (0.6 nm) [42], potentially allowing the tethering of MPD monomers into the MOF pores due to existence of attractive interactions with metal centers. Consequently, this results in the concentration of MPD around the MOF, giving rise to the formation of larger protuberances and also some additional protruding corresponding to the imprint of the own MOF particles below the PA surface.

Fig. 6a reveals that TFN membranes, with the exception of MOF-808@MoS_2, exhibit higher WCA values than TFCs. Although a lower WCA relative to TFC membranes might be anticipated for TFNs due to the hydrophilic behavior of MOF@MoS_2 nanohybrids, the opposite

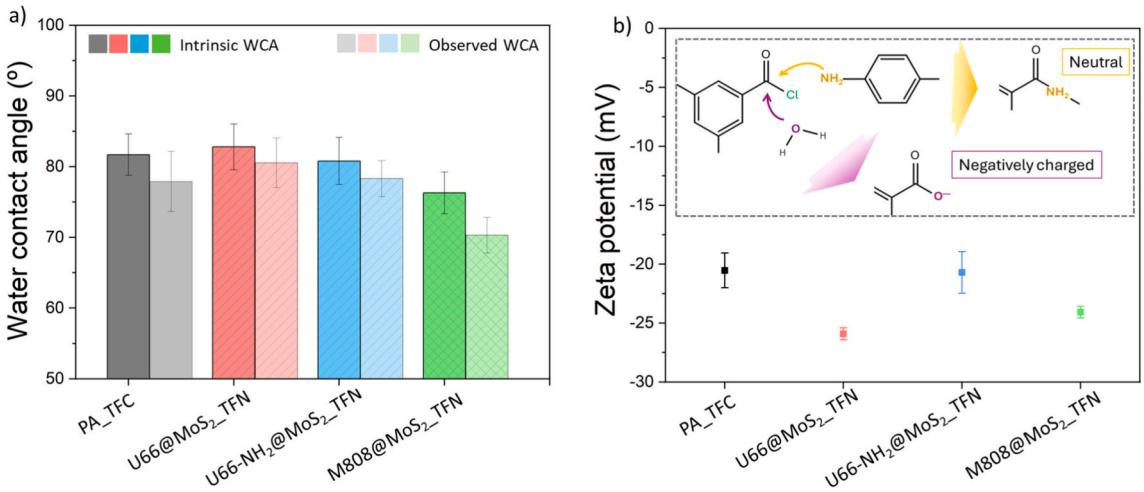

Fig. 6. WCA values (a): intrinsic (dark) and observed (light); intrinsic values correspond to corrected values with Wenzel's equation using AFM roughness, see Table S1. Zeta potential values (b) of TFC and TFNs with UiO-66@MoS_2 (U66@MoS_2_TFN), UiO-66-NH_2@MoS_2 (U66-NH_2@MoS_2_TFN) and MOF-808@MoS_2 (M808@MoS_2_TFN). The dashed inset provides an explanation of the reaction mechanisms that result in the formation of negatively charged membranes.

trend is mainly observed. This discrepancy may be attributed to the presence of MoS_2 nanosheets. These 2D structures alter the membrane surface roughness, creating a smoother outer surface (observed by SEM and AFM). According to the Wenzel and Cassie Baxter equations [43], in a hydrophilic surface (WCA < 90°) the apparent contact angle decreases as the membrane roughness increases. Consequently, in TFNs containing UiO-66@MoS_2 and UiO-66-NH_2@MoS_2 nanohybrids, two opposing effects are observed: (i) the presence of a hydrophilic nanofiller and (ii) a reduction in surface roughness. Moreover, this aligns with the finding that M808@MoS_2_TFN, which shows a comparable surface roughness to TFC, exhibits the lowest WCA among all the membranes evaluated. As explained in the supporting information (eq. S1), corrected WCA values are calculated (Table S1) using the Wenzel equation and the roughness parameters. These results confirm that the corrected (or intrinsic) WCAs for all membranes are higher than the observed WCA in Fig. 6a due to the impact of surface roughness. In addition, those membranes with higher RMS and Ra parameters (TFC and M808@MoS_2_TFN) exhibit more pronounced alterations between the non-corrected and corrected WCAs. The corrected WCA also serves to confirm that the M808@MoS_2_TFN membrane remains as the most hydrophilic membrane, followed by the U66-NH_2@MoS_2_TFN one.

Fig. 6b illustrates the zeta potential measurements of TFC and TFN membranes, accompanied by a schematic representation of the mechanism through which surface charges are generated. During the IP process, MPD and TMC monomers react resulting in a cross-linked PA layer. However, fully cross-linking is not achieved, and unreacted functional groups are present. Unreacted TMC molecules give rise to the formation of negatively charged carboxylic groups, whereas MPD ones remain neutral at the conventional pH operation. Consequently, it is expected a negative charge for the surface of the PA layer (−20.5 mV for the control TFC). The figure shows that the incorporation of the nanohybrids decreases zeta potential, in agreement with more negatively charged surfaces. These findings suggest that the presence of the MOFs impedes the formation of the PA layer during the IP process, resulting in a reduced cross-linked PA layer and the generation of surfaces with a more negative charge [12]; zeta potential values being −25.9 and −24 mV for U66@MoS_2_TFN and M808@MoS_2_TFN, respectively. Both MPD and TMC species can interact with various functional groups in the MOFs; MPD with carboxylic groups and TMC with uncoordinated Zr^{4+}. These competitive interactions hinder efficient PA cross-linking, resulting in unreacted TMC and a negatively charged surface [12,44,45]. This is particularly significant because the presence of ultrasmall MOFs, known by their large surface area to volume ratio and enhanced sorption properties [19], increases the likelihood of interactions with other molecules, inducing additional competing effects to the cross-linking process. Besides monomer-nanohybrid interactions, the presence of unreacted functional groups and defective sites in the MOFs may also contribute to the increase in negative charge [21]. The nanohybrid of UiO-66-NH_2@MoS_2 shows a less negative charge (−20.7 mV) than the other two MOFs, probably due to the presence of the amino group which may react with the carboxylic moieties in TMC (emulating the IP process and consuming TMC) and thus decreasing PA crosslinking.

XPS analysis was performed to confirm the incorporation of the nanohybrids within the TFNs. The detection of zirconium, molybdenum and sulphur in their respective high-resolution spectra (Zr 3d, Mo 3d and S 2p), as illustrated in Fig. S8, indicates the presence of these elements. The relatively low signal intensity is attributed to their encapsulation by the polymer matrix, coupled with the limited penetration depth of XPS (approximately 3–10 nm).

The MWCO of PA TFC and U66@MoS_2_TFN membranes for neutral molecules was assessed using PEG molecules ranging from 200 to 1500 Da (Fig. S9). Both MWCO are around 400 Da (at 90 % rejection) with those of the TFC being slightly lower than those of the TFN. This suggests a more open structure due to the incorporation of MOF@MoS_2 nanohybrids, consistent with the higher water permeance achieved. It is important to note that the MWCO values of both are comparable to those of conventional PA TFC used in NF applications [46].

TEM images of TFN membranes revealed the presence of MOF@MoS_2 nanohybrids located beneath the PA layer (Fig. 7a). Additionally, the characteristic earlike wrinkles typical of this type of polymer films were observed, with the selective PA layer thickness measured at approximately 20 nm (Fig. 7b).

3.3. *Membrane performance*

The NF performance of the membranes incorporating UiO-66@MoS_2, UiO-66-NH_2@MoS_2 and MOF-808@MoS_2 nanofillers was evaluated using solutions of RB, SY and AO. Fig. 8a illustrates the mean permeance and rejection values of TFC and TFN membranes, accompanied by their corresponding standard deviations. The PA_TFC membrane demonstrated a moderate water permeance for RB (5.7 $L{\cdot}m^{-2}{\cdot}h^{-1}{\cdot}bar^{-1}$), SY (5.0 $L{\cdot}m^{-2}{\cdot}h^{-1}{\cdot}bar^{-1}$), and AO (3.9 $L{\cdot}m^{-2}{\cdot}h^{-1}{\cdot}bar^{-1}$) solutions. All TFNs showed an increase in water permeance compared to the control TFC membrane. The incorporation of UiO-66@MoS_2, the nanohybrid with the higher SSA, into the PA matrix (U66@MoS_2_TFN) resulted in a notable enhancement in water

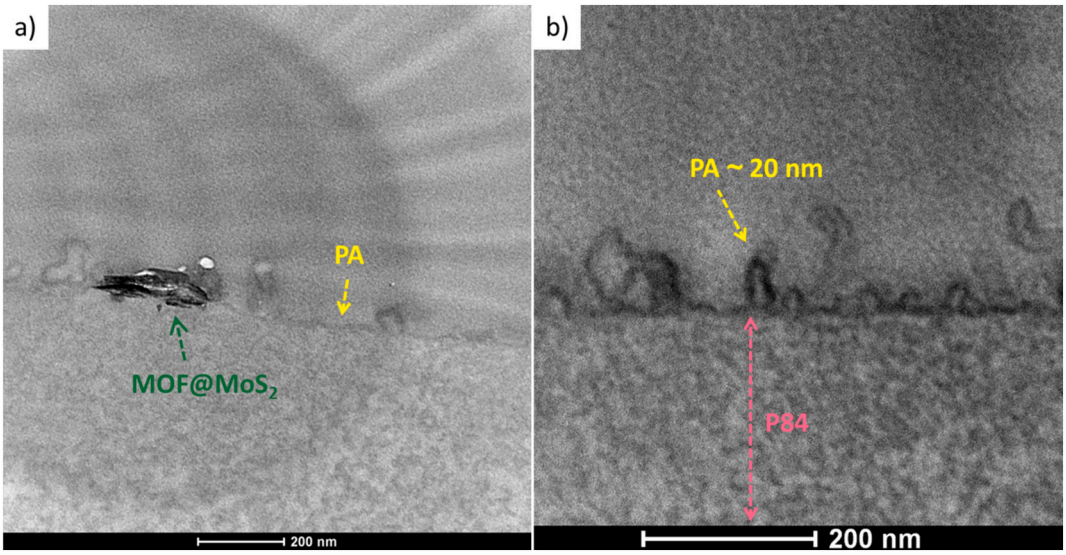

Fig. 7. TEM images of a TFN with UiO-66@MoS_2 (U66@MoS_2_TFN) showing the presence of the nanohybrid (a) and the thickness of the PA selective layer (b).

permeance, particularly for the SY solution, which exhibited an increase to ca. 12 $L{\cdot}m^{-2}{\cdot}h^{-1}{\cdot}bar^{-1}$. The use of UiO-66-$NH_2$@$MoS_2$ nanofiller resulted in a slightly lower permeance compared to U66@MoS_2_TFN, but it still surpassed the control PA_TFC membrane. M808@MoS_2_TFN enhanced the water permeance compared to the control PA_TFC, particularly for RB and AO. The rejection rates remained above 98 % for all dyes, ensuring the efficiency of the TFN membranes in separating the dyes from the aqueous solution. Organic dyes are rejected by membranes primarily through a combination of steric hindrance and electrostatic interactions [47,48]. Large organic dyes such as RB (1017 Da) are likely rejected predominantly due to steric exclusion, as their molecular size exceeds the MWCO of the membranes (see Fig. S9). In contrast, smaller dyes like SY (452 Da) are rejected mainly due to electrostatic repulsion and Donnan effects. Given their negative charge. AO (265 Da), being both small and positively charged, typically presents a challenge for rejection. However, the tight structure of the TFN membranes, along with Donnan exclusion, effectively contributes to its removal [47,49]. Both PA_TFC and all TFN membranes exhibit similarly high rejection for all organic dyes, with differences falling within experimental error. This suggests that dye rejection is primarily governed by the properties of the PA layer. SY exhibits slightly lower rejection compared to RB and AO across all membranes, which may be attributed to differences in interactions with the membrane surface. Theoretically, if the electrostatic repulsion between the negatively charged membrane surface and the negatively charged SY molecules is partially overcome, some SY molecules may pass through due to their smaller size. However, the consistently high rejection values (>98 %) for all membranes indicate that this effect is minimal.

Fig. S10 compares the pure water permeance with that obtained during RB filtration. As expected, for both PA_TFC and U66@MoS_2_TFN, the pure water permeance is higher than that observed in the RB filtration experiments. This difference is attributed to the interaction of dye molecules with the membrane surface, which can block membrane pores and promote concentration polarization. As a result, the local water concentration near the membrane surface decreases, reducing the effective driving force for permeation.

Fig. 8b depicts the water permeance for all bilayered membranes, all of them prepared using UiO-66@MoS_2 nanohybrids. When comparing the two deposition methods, evaporation (Evap) and spin coating (SC), a similar performance was achieved. Spin coating is generally assumed to result in a more homogeneous distribution of 2D nanohybrids, as the spinning forces spread the 2D flakes evenly across the surface. In contrast, during evaporation, the 2D nanohybrids tend to agglomerate. Fig. 8b shows a higher water permeance for BL (Evap) than BL (SC), which can be attributed to the presence of small agglomerates below the PA layer in the former case. These agglomerates may partially hinder the formation of the PA layer around them, introducing additional voids in the membrane, which shortens molecular pathways and enhances water permeation. Despite this, the PA layer can still efficiently remove most organic contaminants, as evidenced by the rejection rates, which exceed 98 % for all tested dyes.

Fig. 8c shows the percentage enhancement in permeance for all membranes (TFNs: filled symbols, bilayer: unfilled symbols). As mentioned above, incorporating MOF@MoS_2 nanohybrids, in both configurations, significantly enhances water permeance. However, bilayered membranes show less improvement compared to the corresponding TFN (U66@MoS_2_TFN). This is likely due to the porous nature of the MOF, promoting the water sorption and passage while restricting the transport of the dye molecules through steric exclusion [12]. Furthermore, the 2D structure of the nanohybrids provides a high surface area-to-volume ratio, thereby increasing the dissemination of ultrasmall NPs of the hydrophilic MOFs along the PA film and, in consequence, the number of sorption sites for water molecules [50,51]. The surface charge, assessed by the measurement of the membrane zeta potential, also influences the NF performance. In general, in NF processes, the use of a membrane with a more negative charge is advantageous, given that the majority of pollutants are negatively charged [52]. This allows for the effective separation of these pollutants from the feed solution through electrostatic repulsion with the membrane surface. Both U66@MoS_2_TFN and M808@MoS_2_TFN exhibited a higher negative charge as compared to control PA_TFC (see Fig. 6b). As seen in Fig. 8c, these two TFNs have the highest increase in permeance for negatively charged dyes (SY and RB), demonstrating the impact of the membrane surface charge. For the positively charged dye AO, due to the counterionic surface charge, AO molecules can interact with the membrane surface, resulting in the deposition of material over the membrane surface. This leads to a reduction in the effective membrane surface area and subsequent inhibition of water transport. M808@MoS_2_TFN exhibited the greatest enhancement in permeance for the AO solution among all TFNs (Fig. 8c), which can be attributed to its higher membrane roughness (see Table S1). A higher surface roughness has the potential to reduce short-range attraction forces with organic molecules [52]. Besides, an increase in membrane roughness results in larger hydrophilic character and membrane surface area features.

The permeance of a given NF membrane is subject to considerable variation depending on the monomers and the synthesis conditions

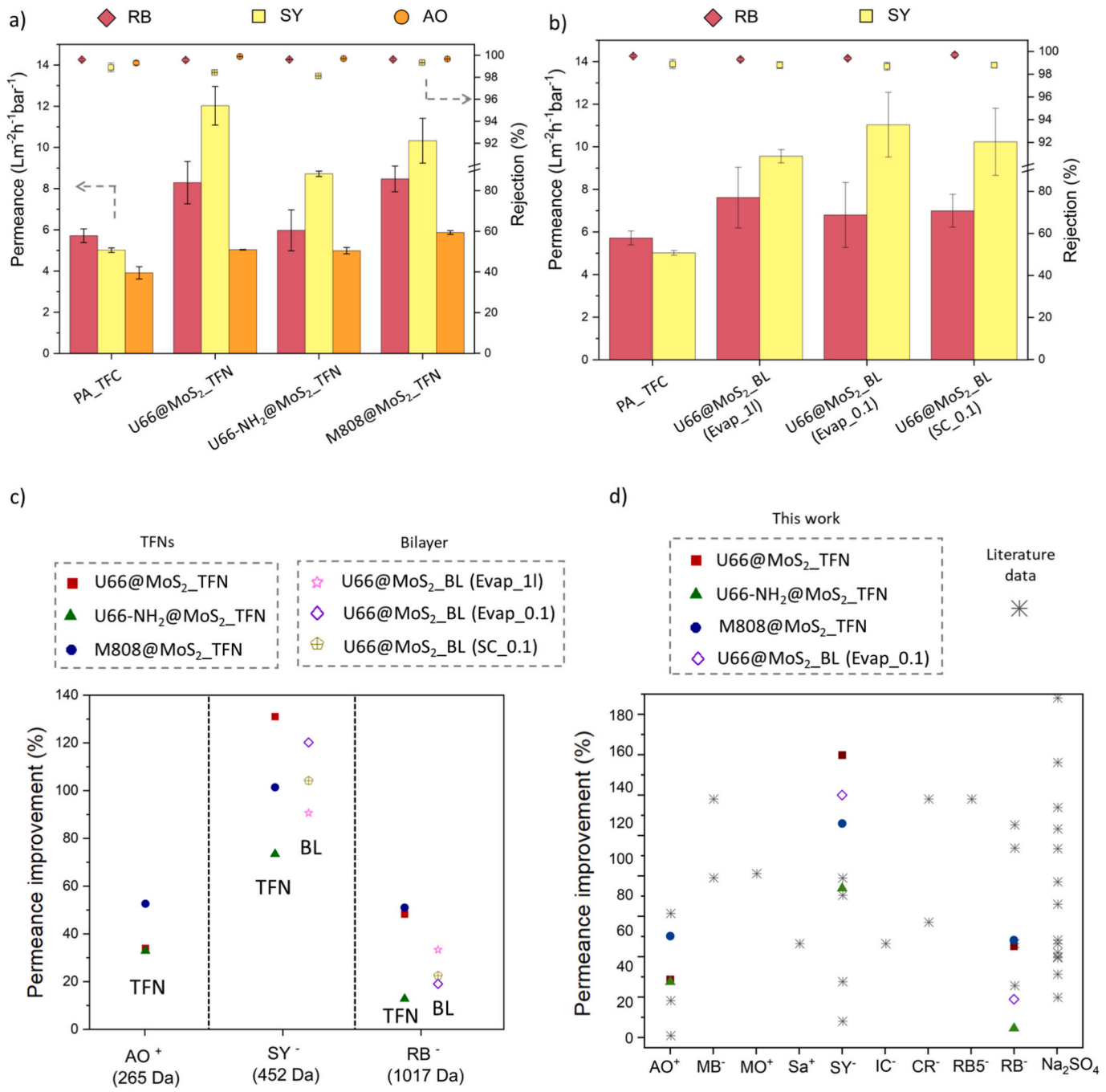

Fig. 8. Permeances and RB, SY and AO rejections of TFN (a) and bilayer (b) membranes together with that of control PA-TFCs. Permeance improvement (as %) for each dye or salt solution of all prepared membranes in this study (c) and comparison with literature values (d). Organic dyes in x axis are ordered from smaller to larger MW and their charge is also included. All the data shown in (d) are provided in the supporting information (Table S2).

employed, along with the characteristics of the polymeric support. Accordingly, when assessing the impact of nanomaterials on the membrane performance, it is imperative to evaluate the enhancement in membrane permeance as compared to the control TFC membrane. Fig. 8d presents a comparative analysis of the permeance improvements observed in our membranes (colored symbols) relative to data from the literature (grey crosses) across a range of dye and salt solutions. In this study, we employed MPD and TMC monomers to fabricate a tight PA layer, which is essential for achieving the required rejection performance across a wide range of dyes, including the particularly challenging positively charged and small AO (265 nm). In contrast, PA layers prepared using other monomers, such as piperazine (PIP), result in more open structures with higher permeances but exhibit a higher MWCO [53] often failing to reject small organic dyes. In addition, we employed a chemically resistant polymeric porous membrane using a commercially available polymer (P84®) with the objective of facilitating the feasibility and scalability of the final membrane. Our membranes exhibit some of the highest permeance increases across the tested solutes, outperforming numerous values reported in the literature, including those corresponding to other TFNs which involve UiO-66 NPs [6,12,44,54,55] or 2D MoS_2 nanosheets [51]. It is important to note that our permeance values correspond to water permeance of dye solutions, whereas some of the literature data reports pure water flux enhancements, which is typically higher due to the absence of pore blocking and concentration

polarization. Our membranes show a particularly noteworthy performance with the negatively charged dye SY, exceeding other reported membranes, e.g. TFNs based on UiO-66-NH_2 NPs [12] and bilayers based on ZIF-8 and ZIF-93 [3].

Compared to commercial membranes with similar MWCO, the membranes reported here exhibit enhanced permeance of 12 $L{\cdot}m^{-2}{\cdot}h^{-1}{\cdot}bar^{-1}$. For example, the NF90 membrane from Dow Filmtec has a water permeance of 8.7 $L{\cdot}m^{-2}{\cdot}h^{-1}{\cdot}bar^{-1}$ [56]. Other commercial membranes, such as NFS and NFX from Synder, show lower water permeance values ranging from 4.2 [57] to 6.3 $L{\cdot}m^{-2}{\cdot}h^{-1}{\cdot}bar^{-1}$ [56]. Similarly, membranes from other manufacturers, such as Veolia, exhibit a water permeance of around 6.5 $L{\cdot}m^{-2}{\cdot}h^{-1}{\cdot}bar^{-1}$ [58].

Membrane recycling was evaluated by testing, then immersing the membrane in DI water for 12 h (overnight), followed by nanofiltration reoperation. As shown in Fig. S11, both PA_TFC and U66@MoS_2_TFN membranes retained their initial water permeance and RB rejection following storage, highlighting their strong potential for industrial applications. Nanofiller leaching is a common concern in TFN membranes, particularly when the fruit of such process is potential pollutant metals. To assess this, the permeate from NF experiments was analyzed using UV–Vis spectroscopy to detect any potential nanofiller UiO-66@MoS_2 release. Fig. S12 presents a comparison among an aqueous dispersion of UiO-66@MoS_2 nanofillers at a concentration of 0.1 $mg \cdot mL^{-1}$, the RB feed solution, and the permeate solution from a U66@MoS_2_TFN membranes. The UV–Vis spectra are consistent with the no noticeable presence of nanofillers in the permeate, suggesting negligible leaching and confirming the stability of the embedded nanofillers during operation. In the unlikely event of UiO-66 detachment from MoS_2 nanosheets, the presence of individual UiO-66 NPs or MoS_2 nanosheets would manifest in the UV–Vis spectrum as a continuous baseline increase, arising from Rayleigh scattering, analogous to that observed for the UiO-66@MoS_2 nanofiller dispersion (blue line).

4. Conclusions

The incorporation of nanosized Zr-based MOFs@MoS_2 nanohybrids produced an enhancement of the NF performance of PA TFC membranes. Three different MOFs, UiO-66, UiO-66-NH_2 and MOF-808, were synthesized onto MoS_2 nanosheets. The utilization of a zirconium oxocluster as the MOF precursor facilitated a precise control over MOF particle size, resulting in the fabrication of ultrasmall nanoparticles with high crystallinity and good textural properties which fully covered the MoS_2 nanosheet.

The nanohybrids were integrated into the PA skin layer in two distinct configurations: (1) The addition of the nanohybrids to the aqueous solution during the IP resulted in the formation of TFN membranes with embedded MOFs@MoS_2 nanosheets within the PA layer. (2) The deposition of the nanohybrids prior to the IP process resulted in the fabrication of bilayered membranes (BL). Membranes were evaluated for water NF of dye (RB, SY and AO) solutions. The membrane performance was shown to be significantly affected by the charge of the dyes. TFNs containing UiO-66@MoS_2 and MOF-808@MoS_2 nanohybrids achieved the highest rejection for negatively charged dyes (SY and RB), which can be attributed to the presence of a more negative surface charge according to zeta potential experiments. The TFN membrane with the highest roughness and hydrophilicity (M808@MoS_2_TFN) exhibited the greatest improvement in permeance for the smallest and positively charged dye (AO). This can be attributed to the less favored interactions between the dye and the membrane surface. All tested TFN and BL membranes exhibited consistent rejection rates above 98 % for all the three dyes, thereby demonstrating their effectiveness for challenging NF applications.

Finally, the prepared membranes were evaluated in comparison with existing literature data. The best performing TFN in this study (containing UiO-66@MoS_2 nanohybrids) exhibited a water permeance of 12 $L{\cdot}m^{-2}{\cdot}h^{-1}{\cdot}bar^{-1}$ and a notable enhancement in permeance of up to 140 % for SY in comparison to the control PA TFC membrane. This extent of permeance improvement is among the highest reported in the literature, with emphasis on the rejection of small molecules, what is key to afford the removal of micropollutants (e.g. drugs, pesticides, etc.). Also, the use of a commercially available polymer (polyimide P84®) paves the way to the scale up of these membranes.

CRediT authorship contribution statement

Javier Colás-Sebastián: Methodology, Investigation, Formal analysis, Data curation. **José Miguel Luque-Alled:** Writing – review & editing, Writing – original draft, Supervision, Project administration, Conceptualization. **Carlos Téllez:** Writing – review & editing, Supervision, Funding acquisition. **Joaquín Coronas:** Writing – review & editing, Supervision, Project administration, Funding acquisition, Conceptualization.

Declaration of competing interest

The authors declare that they have no known competing financial interests or personal relationships that could have appeared to influence the work reported in this paper.

Acknowledgments

Grant PID2022-138582OB-I00 funded by MICIU/AEI/10.13039/501100011033 and by ERDF/EU is gratefully acknowledged ("Agencia Estatal de Investigación" (AEI, Spain), "Ministerio de Ciencia, Innovación y Universidades" (MCIN, Spain) and European Regional Development Fund (ERDF, EU)). J. M. Luque-Alled acknowledges Grant FJC2021-047822-I funded by MICIU/AEI/10.13039/501100011033 and by European Union NextGenerationEU/PRTR. Grants T68_23R and CEX2023-001286-S funded by Government of Aragon and MICIU/AEI/10.13039/501100011033, respectively, are also gratefully acknowledged. Authors would like to acknowledge the use of Servicio General de Apoyo a la Investigación-SAI and the use of instrumentation as well as the technical advice provided by the National Facility ELECMI ICTS, node Laboratorio de Microscopías Avanzadas (LMA), both at the Universidad de Zaragoza.

Appendix A. Supplementary data

Supplementary data to this article can be found online at https://doi.org/10.1016/j.jwpe.2025.108642.

Data availability

No data was used for the research described in the article.

References

[1] M.M. Pendergast, E.M.V. Hoek, A review of water treatment membrane nanotechnologies, Energ. Environ. Sci. 4 (6) (2011) 1946–1971, https://doi.org/10.1039/c0ee00541j.
[2] D.J. Johnson, N. Hilal, Nanocomposite nanofiltration membranes: state of play and recent advances, Desalination 524 (2022), https://doi.org/10.1016/j.desal.2021.115480.
[3] J.M. Luque-Alled, L. Martínez-Izquierdo, P. Gorgojo, C. Téllez, J. Coronas, Organic solvent-free fabrication of thin film polyamide/zeolitic imidazolate framework membranes for removal of dyes from water, Chem. Eng. J. 470 (2023) 144233, https://doi.org/10.1016/j.cej.2023.144233.
[4] L.Y. Wang, M.Q. Fang, J. Liu, J. He, J.D. Li, J.D. Lei, Layer-by-layer fabrication of high-performance polyamide/ZIF-8 nanocomposite membrane for nanofiltration applications, ACS Appl. Mater. Interfaces 7 (43) (2015) 24082–24093, https://doi.org/10.1021/acsami.5b07128.
[5] H. Furukawa, K.E. Cordova, M. O'Keeffe, O.M. Yaghi, The chemistry and applications of metal-organic frameworks, Science 341 (6149) (2013) 974, https://doi.org/10.1126/science.1230444.
[6] X. Zhang, Y.F. Zhang, T.C. Wang, Z. Fan, G.L. Zhang, A thin film nanocomposite membrane with pre-immobilized UiO-66-NH_2 toward enhanced nanofiltration

performance, RSC Adv. 9 (43) (2019) 24802–24810, https://doi.org/10.1039/c9ra04714j.
[7] S. Sorribas, P. Gorgojo, C. Tellez, J. Coronas, A.G. Livingston, High flux thin film nanocomposite membranes based on metal-organic frameworks for organic solvent nanofiltration, J. Am. Chem. Soc. 135 (40) (2013) 15201–15208, https://doi.org/10.1021/ja407665w.
[8] G. Han, R.M. Studer, M. Lee, K. Mizrahi Rodriguez, J.J. Teesdale, Z.P. Smith, Post-synthetic modification of MOFs to enhance interfacial compatibility and selectivity of thin-film nanocomposite (TFN) membranes for water purification, J. Membr. Sci. 666 (2023) 121133, https://doi.org/10.1016/j.memsci.2022.121133.
[9] Y.Q. Lin, H.C. Wu, Q. Shen, L. Zhang, K.C. Guan, T. Shintani, K.L. Tung, T. Yoshioka, H. Matsuyama, Custom-tailoring metal-organic framework in thin-film nanocomposite nanofiltration membrane with enhanced internal polarity and amplified surface crosslinking for elevated separation property, Desalination 493 (2020), https://doi.org/10.1016/j.desal.2020.114649.
[10] J. Winarta, B.H. Shan, S.M. McIntyre, L. Ye, C. Wang, J.C. Liu, B. Mu, A decade of UiO-66 research: a historic review of dynamic structure, synthesis mechanisms, and characterization techniques of an archetypal metal-organic framework, Cryst. Growth Des. 20 (2) (2020) 1347–1362, https://doi.org/10.1021/acs.cgd.9b00955.
[11] D.C. Ma, S.B. Peh, G. Han, S.B. Chen, Thin-film nanocomposite (TFN) membranes incorporated with super-hydrophilic metal- organic framework (MOF) UiO-66: toward enhancement of water flux and salt rejection, ACS Appl. Mater. Interfaces 9 (8) (2017) 7523–7534, https://doi.org/10.1021/acsami.6b14223.
[12] F. Aghili, A.A. Ghoreyshi, B. Van der Bruggen, A. Rahimpour, Introducing gel-based UiO-66-NH_2 into polyamide matrix for preparation of new super hydrophilic membrane with superior performance in dyeing wastewater treatment, J. Environ. Chem. Eng. 9 (4) (2021), https://doi.org/10.1016/j.jece.2021.105484.
[13] K.D. Nguyen, N.T. Vo, K.T.M. Le, K.V. Ho, N.T.S. Phan, P.H. Ho, H.V. Le, Defect-engineered metal-organic frameworks (MOF-808) towards the improved adsorptive removal of organic dyes and chromium (vi) species from water, New J. Chem. 47 (13) (2023) 6433–6447, https://doi.org/10.1039/d2nj05693c.
[14] I. del Castillo-Velilla, A. Sousaraei, I. Romero-Muñiz, C. Castillo-Blas, A.S. J. Méndez, F.E. Oropeza, V.A.D. O'Shea, J. Cabanillas-González, A. Mavrandonakis, A.E. Platero-Prats, Synergistic binding sites in a metal-organic framework for the optical sensing of nitrogen dioxide, Nat. Commun. 14 (1) (2023), https://doi.org/10.1038/s41467-023-38170-9.
[15] Z. Li, W. Zhang, M. Tao, L. Shen, R. Li, M. Zhang, Y. Jiao, H. Hong, Y. Xu, H. Lin, In-situ growth of UiO-66-NH_2 in porous polymeric substrates at room temperature for fabrication of mixed matrix membranes with fast molecular separation performance, Chem. Eng. J. 435 (2022), https://doi.org/10.1016/j.cej.2022.134804.
[16] J. Zhu, X. Meng, W. Liu, Y. Qi, S. Jin, S. Huo, Regulated synthesis of Zr-metal-organic frameworks with variable hole size and its influence on the performance of novel MOF-based heterogeneous amino acid-thiourea catalysts, RSC Adv. 12 (33) (2022) 21574–21581, https://doi.org/10.1039/d2ra03747e.
[17] A. Kazemi, F. Moghadaskhou, M. Pordsari, F. Manteghi, A. Tadjarodi, A. Ghaemi, Enhanced CO_2 capture potential of UiO-66-NH_2 synthesized by sonochemical method: experimental findings and performance evaluation, Sci. Rep. 13 (1) (2023), https://doi.org/10.1038/s41598-023-47221-6.
[18] B.Y. Qiu, M. Yu, J.M. Luque-Alled, S.Z. Ding, A.B. Foster, P.M. Budd, X.L. Fan, P. Gorgojo, High gas permeability in aged superglassy membranes with nanosized UiO-66-NH_2/cPIM-1 network fillers, Angew. Chem. Int. Ed. (2023), https://doi.org/10.1002/anie.202316356.
[19] L. Martínez-Izquierdo, C. García-Comas, S. Dai, M. Navarro, A. Tissot, C. Serre, C. Téllez, J. Coronas, Ultrasmall functionalized UiO-66 nanoparticle/polymer Pebax 1657 thin-film nanocomposite membranes for optimal CO_2 separation, ACS Appl. Mater. Interfaces 16 (3) (2024) 4024–4034, https://doi.org/10.1021/acsami.3c16093.
[20] S. Dai, C. Simms, G. Patriarche, M. Daturi, A. Tissot, T.N. Parac-Vogt, C. Serre, Highly defective ultra-small tetravalent MOF nanocrystals, Nat. Commun. 15 (1) (2024), https://doi.org/10.1038/s41467-024-47426-x.
[21] J.H. Yan, Y.W. Sun, T.T. Ji, C.H. Zhang, L.L. Liu, Y. Liu, Room-temperature synthesis of defect-engineered zirconium-MOF membrane enabling superior CO_2/N_2 selectivity with zirconium-oxo cluster source, J. Membr. Sci. 653 (2022), https://doi.org/10.1016/j.memsci.2022.120496.
[22] H.H. Su, J.W. Hou, J.Y. Zhu, Y.T. Zhang, B. van der Bruggen, Room-temperature aqueous synthesis of MOF-808(Zr) for selective adsorption of dye mixtures, Sep. Purif. Technol. 333 (2024), https://doi.org/10.1016/j.seppur.2023.125957.
[23] Y.Q. Gong, S.J. Gao, Y.Y. Tian, Y.Z. Zhu, W.X. Fang, Z.G. Wang, J. Jin, Thin-film nanocomposite nanofiltration membrane with an ultrathin polyamide/UIO-66-NH_2 active layer for high-performance desalination, J. Membr. Sci. 600 (2020), https://doi.org/10.1016/j.memsci.2020.117874.
[24] X.R. Gao, P. Li, Z.Y. Gu, Q. Xiao, S.L. Yu, L.A. Hou, Preparation of poly(piperazine-amide) nanofilms with micro-wrinkled surface via nanoparticle-templated interfacial polymerization: performance and mechanism, J. Membr. Sci. 638 (2021), https://doi.org/10.1016/j.memsci.2021.119711.
[25] F. Xie, W. Li, X. Gong, D. Taymazov, H. Ding, H. Zhang, X. Ma, Z. Xu, MoS_2 @PDA thin-film nanocomposite nanofiltration membrane for simultaneously improved permeability and selectivity, J. Environ. Chem. Eng. 10 (2022), https://doi.org/10.1016/j.jece.2022.107697.
[26] J. Zhu, W. Meng, Q. Xue, K. Zhang, Two dimensional sulfonated molybdenum disulfide (S-MoS_2) thin-film nanocomposite nanofiltration membrane for selective desalination, J. Membr. Sci. 676 (2023), https://doi.org/10.1016/j.memsci.2023.121574.
[27] M. Ma, C. Zhang, C. Zhu, S. Huang, J. Yang, Z. Xu, Nanocomposite membranes embedded with functionalized MoS_2 nanosheets for enhanced interfacial compatibility and nanofiltration performance, J. Membr. Sci. 591 (2019), https://doi.org/10.1016/j.memsci.2019.117316.
[28] X. Wang, Y. Liu, K. Fan, P. Cheng, S. Xia, L. Qian, Construction of thin-film nanocomposite membranes by incorporating acyl chloride@MoS_2 for enhanced nanofiltration performance, Sep. Purif. Technol. 319 (2023), https://doi.org/10.1016/j.seppur.2023.124078.
[29] J.M. Luque-Alled, C. Moreno, P. Gorgojo, Two-dimensional materials for gas separation membranes, Curr. Opin. Chem. Eng. 39 (2023), https://doi.org/10.1016/j.coche.2023.100901.
[30] Y. Li, X. Zhang, A. Yang, C.Y. Jiang, G.L. Zhang, J.W. Mao, Q. Meng, Polyphenol etched ZIF-8 modified graphene oxide nanofiltration membrane for efficient removal of salts and organic molecules, J. Membr. Sci. 635 (2021), https://doi.org/10.1016/j.memsci.2021.119521.
[31] S.Y. Fang, J.L. Gong, L. Tang, W.C. Cao, J. Li, Z.K. Tan, Q.Y. Niu, Z.P. Chen, Construction the hierarchical architecture of molybdenum disulfide/MOF composite membrane via electrostatic self-assembly strategy for efficient molecular separation, Chem. Eng. J. 449 (2022), https://doi.org/10.1016/j.cej.2022.137808.
[32] S. Castarlenas, C. Tellez, J. Coronas, Gas separation with mixed matrix membranes obtained from MOF UiO-66-graphite oxide hybrids, J. Membr. Sci. 526 (2017) 205–211, https://doi.org/10.1016/j.memsci.2016.12.041.
[33] J.Q. Wang, L. Wang, M.L. He, X.D. Wang, Y.T. Lv, D.X. Huang, J. Wang, R. Miao, L. J. Nie, J.J. Hao, Highly permeable thin film nanocomposite membrane utilizing a MoS_2@NH_2-UiO-66 interlayer for forward osmosis removal of CO_3^{2-}, Sr^{2+} and Cs^+ nuclide ions, Appl. Surf. Sci. 611 (2023), https://doi.org/10.1016/j.apsusc.2022.155618.
[34] L. Martínez-Izquierdo, C. García-Comas, S. Dai, M. Navarro, A. Tissot, C. Serre, C. Téllez, J. Coronas, Ultrasmall functionalized UiO-66 nanoparticle/polymer Pebax 1657 thin-film nanocomposite membranes for optimal CO_2 separation, ACS Appl. Mater. Interfaces (2024) 4024–4034, https://doi.org/10.1021/acsami.3c16093.
[35] J. Sun, M. Yan, G. Tao, R. Su, X. Xiao, Q. Wu, F. Chen, X. Wu, H. Lin, A single-atom manganese nanozyme mediated membrane reactor for water decontamination, Water Res. 268 (2025), https://doi.org/10.1016/j.watres.2024.122627.
[36] X. Wang, S. Seyedpour, S. Hrapovic, U. Hemraz, M. Mozafari, M. Soroush, M. Islam, A. Mollahosseini, M. Sadrzadeh, J. Cho, Ultra-small defect-engineered UiO-66 on cellulose nanocrystal template for advanced carbon dioxide capture membrane, Clean. Eng. Technol. 27 (2025), https://doi.org/10.1016/j.clet.2025.100999.
[37] C. Quilty, L. Housel, D. Bock, M. Dunkin, L. Wang, D. Lutz, A. Abraham, A. Bruck, E. Takeuchi, K. Takeuchi, A. Marschilok, Ex situ and operando XRD and XAS analysis of MoS_2: a lithiation study of bulk and nanosheet materials, ACS Appl Energy Mater 2 (2019) 7635–7646, https://doi.org/10.1021/acsaem.9b01538.
[38] S. Dai, F. Nouar, S. Zhang, A. Tissot, C. Serre, One-step room-temperature synthesis of metal(IV) carboxylate metal-organic frameworks, Angew. Chem. Int. Ed. 60 (2021) 4282–4288, https://doi.org/10.1002/anie.202014184.
[39] S. Hussain, J. Singh, D. Vikraman, A. Singh, M. Iqbal, M. Khan, P. Kumar, D. Choi, W. Song, K. An, J. Eom, W. Lee, J. Jung, Large-area, continuous and high electrical performances of bilayer to few layers MoS_2 fabricated by RF sputtering via post-deposition annealing method, Sci. Rep. 6 (2016), https://doi.org/10.1038/srep30791.
[40] C. Van Goethem, R. Verbeke, S. Hermans, R. Bernstein, I.F.J. Vankelecom, Controlled positioning of MOFs in interfacially polymerized thin-film nanocomposites, J Mater Chem A 4 (42) (2016) 16368–16376, https://doi.org/10.1039/c6ta05175h.
[41] Y.Y. Zhao, Y.L. Liu, X.M. Wang, X. Huang, Y.F.F. Xie, Impacts of metal-organic frameworks on structure and performance of polyamide thin-film nanocomposite membranes, ACS Appl. Mater. Interfaces 11 (14) (2019) 13724–13734, https://doi.org/10.1021/acsami.9b01923.
[42] G. Robertson, S. Mosca, C. Castillo-Blas, F. Son, O. Farha, D. Keen, S. Anzellini, T. Bennett, Survival of zirconium-based metal-organic framework crystallinity at extreme pressures, Inorg. Chem. 62 (2023) 10092–10099, https://doi.org/10.1021/acs.inorgchem.2c04428.
[43] H.Y. Erbil, C.E. Cansoy, Range of applicability of the Wenzel and Cassie−Baxter equations for superhydrophobic surfaces†, Langmuir 25 (24) (2009) https://doi.org/10.1021/la902098a.
[44] L. Ni, Z. Liao, K. Chen, J. Xie, Q. Li, J. Qi, X. Sun, L. Wang, J. Li, Defect-engineered UiO-66-NH_2 modified thin film nanocomposite membrane with enhanced nanofiltration performance, Chem. Commun. 56 (2020) 8372–8375, https://doi.org/10.1039/d0cc01556c.
[45] F. Aghili, A. Ghoreyshi, B. Van der Bruggen, A. Rahimpour, A highly permeable UiO-66-NH_2/polyethyleneimine thin-film nanocomposite membrane for recovery of valuable metal ions from brackish water, Process Saf. Environ. Prot. 151 (2021) 244–256, https://doi.org/10.1016/j.psep.2021.05.022.
[46] V.T. Do, C.Y. Tang, M. Reinhard, J.O. Leckie, Effects of hypochlorous acid exposure on the rejection of salt, polyethylene glycols, boron and arsenic(V) by nanofiltration and reverse osmosis membranes, Water Res. 46 (16) (2012) 5217–5223, https://doi.org/10.1016/j.watres.2012.06.044.
[47] Y. Liu, S. Liang, Y. Qian, H. Zuo, M. Duan, A loose nanofiltration membrane prepared by interfacial radical polymerization for dye/salt separation, J. Membr. Sci. 701 (2024), https://doi.org/10.1016/j.memsci.2024.122751.
[48] F. Donnan, Theory of membrane equilibria and membrane-potentials in the presence of non-dialyzing electrolytes - a contribution to physical-chemical physiology (reprinted from zeitshrift fur elektrochemie und angewandte physikalische chemie, VOL 17, PG 572, 1911), J. Membr. Sci. 100 (1) (1995) 45–55, https://doi.org/10.1016/0376-7388(94)00297-C.

[49] C. Pina-Vidal, J. Luque-Alled, J. Coronas, C. Téllez, Sustainable ß- and ?-cyclodextrins for development of highly permeable thin film composite nanofiltration membranes, Mater. Today Sustain. 24 (2023) 100593, https://doi.org/10.1016/j.mtsust.2023.100593.
[50] S. Yang, Q. Jiang, K. Zhang, Few-layers 2D o-MoS_2 TFN nanofiltration membranes for future desalination, J. Membr. Sci. 604 (2020), https://doi.org/10.1016/j.memsci.2020.118052.
[51] S. Liu, E. Wang, X. Lv, L. Liu, B. Su, L. Han, High performance internally pressurized hollow fiber thin-film nanocomposite nanofiltration membrane incorporated with tannic acid functionalized MoS_2 nanosheets for wastewater treatment, DESALINATION 547 (2023), https://doi.org/10.1016/j.desal.2022.116227.
[52] D. Rana, T. Matsuura, Surface modifications for antifouling membranes, Chem. Rev. 110 (4) (2010) 2448–2471, https://doi.org/10.1021/cr800208y.
[53] S. Karan, Z.W. Jiang, A.G. Livingston, Sub-10 nm polyamide nanofilms with ultrafast solvent transport for molecular separation, Science 348 (6241) (2015) 1347–1351, https://doi.org/10.1126/science.aaa5058.
[54] D. Zhao, H. Jin, Q. Zhao, Y. Xu, L. Shen, H. Lin, T. Chung, Smart integration of MOFs and CQDs to fabricate defect-free and self-cleaning TFN membranes for dye removal, J. Membr. Sci. 679 (2023), https://doi.org/10.1016/j.memsci.2023.121706.
[55] Z. Gu, S. Yu, J. Zhu, P. Li, X. Gao, R. Zhang, Incorporation of lysine-modified UiO-66 for the construction of thin-film nanocomposite nanofiltration membrane with enhanced water flux and salt selectivity, Desalination 493 (2020), https://doi.org/10.1016/j.desal.2020.114661.
[56] R. Zylla, M. Foszpanczyk, I. Kaminska, M. Kudzin, J. Balcerzak, S. Ledakowicz, Impact of polymer membrane properties on the removal of pharmaceuticals, Membranes 12 (2) (2022), https://doi.org/10.3390/membranes12020150.
[57] A. Premachandra, C. Michaud-Lavoie, B. Chester, M. McClure, I. Sarkar, K. Lutes, S. Rollings-Scattergood, D. Latulippe, Development of a crossflow nanofiltration process for polishing of wastewater by-product from biogas production processes, J. Water Process Eng. 50 (2022), https://doi.org/10.1016/j.jwpe.2022.103197.
[58] L. Liu, Y. Liu, X. Chen, S. Feng, Y. Wan, H. Lu, J. Luo, A nanofiltration membrane with outstanding antifouling ability: exploring the structure-property-performance relationship, J. Membr. Sci. 668 (2023), https://doi.org/10.1016/j.memsci.2022.121205.